Solar Coronal Heating by Kinetic Alfvén Waves

Syed Ayaz[1] , Gang Li[1,2] , and Imran A. Khan[3,4]
[1] Department of Space Science and CSPAR, University of Alabama in Huntsville, Huntsville, AL 35899, USA
[2] General Linear Space Plasma Lab LLC, Foster City, CA 94404, USA
[3] Department of Space Sciences, Institute of Space Technology, Islamabad 44000, Pakistan
[4] Space and Astrophysics Research Lab (SARL), National Center of GIS and Space Applications (NCGSA), Islamabad 44000, Pakistan

Abstract

The utilization of the Cairns distribution serves as a vital tool for characterizing the nonthermal attributes commonly observed in space plasmas. In these intricate plasma environments, extensive measurements have been conducted to monitor the fluctuations inherent in the perturbed electromagnetic (EM) field and the associated Poynting flux, specifically concerning kinetic Alfvén waves (KAWs). Traditionally, these fluctuations have been attributed to gyroradius correction terms within the framework of Maxwellian distributed plasmas. However, our study introduces an innovative perspective grounded in kinetic theory coupled with the Cairns distribution, adept at encapsulating the nonthermal nuances characterized by the index parameter Λ. Within the domain of the solar corona, our investigation centers on the perturbed EM field ratios and the Poynting flux of KAWs, with a foundation in the Cairns distribution function. It is noteworthy that the perpendicular components, although deemed less significant due to the dominance of $k_\perp$ over $k_\parallel$, remain unquantified regarding their relative insignificance. Similarly, the exploration of the imaginary part of the normalized EM field ratio has been a relatively understudied domain. Furthermore, we delve into the nuanced assessment of the power rate I_x/I_z characterizing the perpendicular and parallel normalized Poynting fluxes (S_x and S_z). Intriguingly, we discern that large values of Λ, compared to their Maxwellian counterparts, manifest advantageous attributes, particularly concerning the energization of the plasma over extended distances along the ambient magnetic field lines. The analytical insights gleaned from this study find practical application in understanding phenomena within the solar atmosphere, particularly shedding light on the significant role played by nonthermal particles in the observed heating processes.

Unified Astronomy Thesaurus concepts: Solar coronal heating (1989)

1. Introduction

The solar corona, an ethereal and enigmatic region surrounding the Sun, represents a remarkable component of our star's atmosphere. Extending far beyond the visible disk of the Sun, the corona is characterized by its extraordinarily high temperatures, often exceeding 10^6 K (De Moortel & Browning 2015). The perplexing existence of this counterintuitive high-temperature corona above the photosphere has captivated the attention of astrophysicists for nearly seven decades, giving rise to what is now known as the "solar coronal heating problem." We delve into the historical context of this problem and explore recent findings related to the role of perturbed electromagnetic (EM) fields and Poynting flux phenomena of kinetic Alfvén waves (KAWs) in the corona's complex physics. KAWs have been the focus of comprehensive investigations in space, particularly in the solar wind and solar corona, as well as in laboratory settings such as fusion reactors, and other astrophysical environments (Cramer 2011; Wu et al. 2020). Researchers have explored KAWs through a multifaceted approach encompassing experimental studies, rigorous theoretical analyses, sophisticated simulations, and practical applications in plasma heating and particle acceleration. A wealth of valuable insights into this intricate phenomenon can be found in the review articles (for details, see Gekelman (1999), Stasiewicz et al. (2000),

Wu & Chao (2004), Keiling (2009), and Zhao et al. (2010)) and references therein).

It is commonly known that space plasmas exhibit a range of waves, among which KAWs hold particular significance (Cramer 2011; Wu et al. 2020). The pioneering work of Hasegawa & Chen (1976) established Alfvén waves, KAWs in particular, as a standard reference in the field of space plasmas. KAWs are defined as Alfvén waves with a perpendicular wavelength comparable to the ion gyroradius. Observations from several spacecraft have demonstrated that KAWs dissipate and contribute to plasma heating during their propagation (Wygant et al. 2000, 2002; Lysak & Song 2003; Gershman et al. 2017). These waves play a crucial role in the transport, heating, and acceleration mechanisms within space and astrophysical environments. Notably, the experimental investigation of KAWs gained momentum with the establishment of the Large Plasma Device (LAPD) at the University of California, Los Angeles, in 1989. A series of experiments conducted on KAWs in the LAPD revealed striking similarities to the observations made by satellites in space plasma since 1990.

Extensive observations from spacecraft have consistently demonstrated that space and astrophysical plasmas are predominantly collisionless and exhibit deviations from thermal equilibrium (Khan & Murtaza 2018 and references therein). These nonthermal characteristics, usually deviating from Maxwellian, are often observed in nonmonotonic velocity distributions, an abundance of suprathermal particles, and high-energy tails, particularly in space plasmas such as the solar wind. To effectively model these deviations from the Maxwellian distribution, various non-Maxwellian distributions

have been proposed (Cairns et al. 1995; Pierrard & Lazar 2010; Liu et al. 2014; Rubab et al. 2014; Zank 2017; Barik et al. 2020, 2024). Among these distributions, the Cairns distribution (Cairns et al. 1995) offers a straightforward analytical choice. Cairns et al. (1995) introduced this distribution to study the energetic ion solitary structures in the upper ionosphere. The distribution has been validated by consistent observations made by the Freja (Bostrom 1992) and Viking (Dovner et al. 1994) satellites. In the Cairns distribution function, the nonthermal parameter Λ plays a vital role; it controls the nonthermal properties of the plasma system, determining the population of free electrons and shaping the distribution function. Importantly, the Cairns distribution serves as a good theoretical tool to explain a wide range of nonthermal phenomena observed in space plasmas (Verheest & Pillay 2008; Khan et al. 2018; Ayaz et al. 2019, 2020). Therefore, we have chosen to employ the Cairns distribution in this research due to its remarkable applicability in the study of the solar atmosphere. Moreover, considering the simultaneous existence of KAWs and non-thermal particles in space plasmas, it is reasonable to anticipate the impact of the Cairns distribution on the dynamics of KAWs. Extensive scientific investigations have demonstrated the influence of the Cairns distribution (or closely related distributions) on the damping of KAWs (Liu et al. 2014; Khan et al. 2020; Khalid et al. 2022). In our previous studies (Ayaz et al. 2019, 2020), we specifically examined the role of the Cairns parameter Λ in shaping the damping behavior of KAWs. Our findings revealed that KAWs experience damping in the presence of the perpendicular wavenumber ($k_\perp \rho_i$), with the spectral index Λ playing a significant role in conjunction with $k_\perp \rho_i$.

In general, the damping rate characterizes the rate of energy conversion of a wave, such as KAWs under consideration, into other forms, including plasma heating or particle acceleration. However, the damping expression alone does not provide sufficient insight into how the wave transfers its energy to the plasma during propagation in space. This critical information can be obtained through the examination of the Poynting flux vector, which necessitates knowledge of the perturbed EM fields associated with KAWs. The perturbed electric and magnetic fields play a pivotal role in comprehending the phenomena related to the Poynting flux of KAWs. Notably, the study of KAWs has garnered significant attention, particularly with the availability of spacecraft observations that directly measure the perturbed fields (Wygant et al. 2000; Lysak & Song 2003; Lysak 2023). The identification of KAWs in space plasmas can be achieved theoretically by examining the ratio and phase relationship between the two perturbed fields. In this context, the damping rate serves as a useful tool for simplifying the determination of the Poynting flux associated with KAWs.

To understand this puzzling scenario of KAWs in space and astrophysical contexts, several mechanisms have been suggested so far (see reviews in Lakhina 1990, 2008; Nishizuka et al. 2008; Barik et al. 2019a, 2019b, 2019c). Previous studies have primarily focused on the Maxwellian distribution, attributing the fluctuations to gyroradius correction terms. Khan (2019) investigated KAWs within the context of the kappa distribution and highlighted the significance of small values of the index κ compared to the Maxwellian case in terms of energy transport by KAWs. It is found that the Poynting flux vector of KAWs decays at a faster rate as the values of the index κ increase. In recent studies by Barik et al. (2020, 2024),

KAWs have also been investigated using the κ distribution together with Maxwellian. Intriguingly, these works reveal that the excitation of waves solely by velocity shear leads to the emergence of purely growing KAWs within the auroral region of Earth's magnetosphere. This finding not only sheds light on the complex dynamics of KAWs in specific geophysical contexts but also highlights their potential applicability across diverse plasma environments. Indeed, the insights gained from this research extend beyond the confines of the auroral region to encompass other regions of the magnetosphere, the solar wind, and the interplanetary medium. These findings underscore the universal relevance of ion beam signatures, velocity shear effects, and the presence of non-Maxwellian electron distributions in shaping wave phenomena and plasma dynamics throughout the vast reaches of space.

In the present investigation, we consider the Cairns distribution function to study the behavior of KAWs in the coronal plasma. Our investigation explores the influence of the index parameter Λ on the perturbed EM field, the Poynting flux, and the power delivery rate of KAWs in the solar atmosphere. To the best of our knowledge, this is the first report on these topics. The structure of the paper is organized as follows. Section 2 presents the analytical model, Section 3 provides graphical demonstrations of the results, and Section 4 presents the corresponding discussion based on the findings. Finally, the analytical results are concluded in Section 5.

2. Analytical Model

We derived the analytical expressions for the perturbed EM fields (electric and magnetic) and the Poynting flux vector associated with KAWs by considering the following assumptions: the plasma is collisionless and homogeneous, with electrons and ions following the Cairns velocity distribution function. Furthermore, the magnetic pressure is larger than the thermal pressure (i.e., $\beta_p \ll 1$), and the plasma supports low-frequency waves, by which we mean the wave frequency is lower than the ion gyrofrequency ($\omega < \Omega_i$). In the geometry of Figure 1, the wave is emitted from a source located at $z = 0$, the ambient magnetic field (B_0) is along the z-axis, the perturbed field (B_y) is along the y-axis, and the electric field and wavevector lie in the x–z plane. In this research, we are investigating KAWs in the solar corona; particularly, we set the simple geometry of obliquely propagating KAWs in the solar flux tube loop shown in Figure 1 (right). As stated earlier, the plasma is out of thermal equilibrium, i.e., nonthermal features are present that are different from Maxwellian. To model such a plasma system, we need a distribution function $f_{0s}(v)$, and our chosen distribution is the Cairns distribution of the following form:

$$f_{0s}(v) = \frac{1}{(1 + \Lambda \frac{15}{4})\pi^{3/2} v_{ts}^3}\left(1 + \Lambda \frac{v^4}{v_{ts}^4}\right)e^{-\frac{v^2}{v_{ts}^2}}. \qquad (1)$$

Here $v_{ts} = \sqrt{\frac{2T_s}{m_s}}$ is the thermal velocity of s species (s being electrons or ions) having temperature T_s and mass m_s. The spectral index Λ having values $\Lambda \geqslant 0$ controls the nonthermal features of the plasma system. For $\Lambda = 0$, Equation (1) reduces to the Maxwellian distribution function.
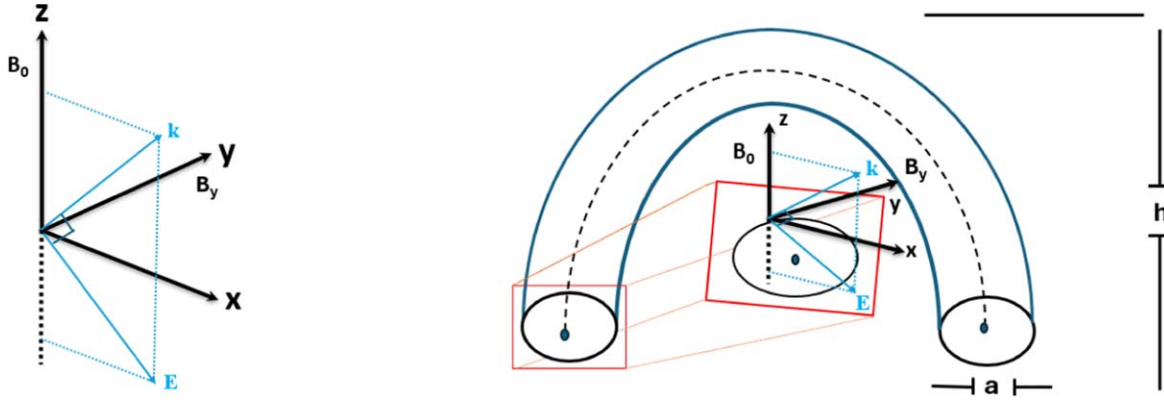
Figure 1. Geometry of the system. (Left) Obliquely propagating KAWs. (Right) Fitted geometry in the solar flux tube loop of height h having a circular cross section of radius a.

2.1. Dispersion Relations of KAWs

In the domain of kinetic plasma theory, from the Vlasov–Maxwell equation, the dispersion relation for EM waves takes the form (Lysak & Lotko 1996; Lysak 1998; Barik et al. 2023)

$$\begin{pmatrix} \epsilon_{xx} - \frac{k_\parallel^2 c^2}{\omega^2} & \frac{k_\perp k_\parallel c^2}{\omega^2} \\ \frac{k_\perp k_\parallel c^2}{\omega^2} & \epsilon_{zz} - \frac{k_\perp^2 c^2}{\omega^2} \end{pmatrix} \begin{pmatrix} E_x \\ E_z \end{pmatrix} = 0, \qquad (2)$$

where ϵ_{xx} and ϵ_{zz} are components of the permittivity tensor, $k_\parallel$ and $k_\perp$ are the wavevectors parallel and perpendicular to B_0, ω is the angular frequency, and c is the speed of light. We assume that ω is a complex quantity, i.e., $\omega = \omega_R + i\omega_i$ with $\omega_i \ll \omega_R$, where the subscripts R and i denote real and imaginary, respectively.

The components of the permittivity tensors (ϵ_{xx} and ϵ_{zz}) in cylindrical coordinates are related to the distribution function through

$$\epsilon_{xx} = 1 + \sum_s \frac{\omega_{ps}^2}{\omega} \int d^3v \sum_{n=-\infty}^{\infty} \frac{n^2}{\zeta_s^2} \frac{v_\perp J_n^2(\zeta_s)}{(\omega - k_\parallel v_\parallel - n\Omega_s)} \frac{\partial f_0(v)}{\partial v_\perp} \qquad (3)$$

and

$$\epsilon_{zz} = 1 + \sum_s \frac{\omega_{ps}^2}{\omega} \int d^3v \sum_{n=-\infty}^{\infty} \frac{J_n^2(\zeta_s)}{(\omega - k_\parallel v_\parallel - n\Omega_s)} \frac{v_\parallel^2}{v_\perp} \frac{\partial f_0(v)}{\partial v_\perp}, \qquad (4)$$

where the plasma and gyrofrequencies are $\omega_{ps} = \sqrt{4\pi n_0 e^2/m_s}$ and $\Omega_s = q_s B_0/m_s c$, respectively. In the above equations, $J_n(\zeta_s)$ is the Bessel function with an argument $\zeta_s = k_\perp v_\perp/\Omega_s$. In Equations (3) and (4), we consider $f_{0s}(v)$ to be the Cairns distribution (Equation (1)). Using $f_{0s}(v)$ in these two equations and solving the parallel and perpendicular integrals with the assumption that the ion gyroradius is smaller than the perpendicular wavelength (i.e., $k_\perp \rho_i \ll 1$), we get (Ayaz et al. 2019, 2020)

$$\epsilon_{xx} = \frac{1}{\left(1 + \Lambda \frac{15}{4}\right)} \frac{c^2}{v_A^2} \left(1 - \frac{3}{4} k_\perp^2 \rho_i^2 + \frac{\Lambda}{4}\right) \qquad (5)$$

and

$$\epsilon_{zz} = -\frac{1}{\left(1 + \Lambda \frac{15}{4}\right)} \left(\frac{Z'(\xi_e)}{2k_\parallel^2 \lambda_{De}^2} + \frac{Z'(\xi_i)}{2k_\parallel^2 \lambda_{Di}^2}\right), \qquad (6)$$

where $v_A = \frac{B_0}{\sqrt{4\pi n_0 m_i}}$ is Alfvénic speed, $\rho_i^2(=v_{ti}^2/2\Omega_i^2)$ is the ion gyroradius, $\lambda_{De,i}(=v_{te,i}/\sqrt{2}\,\omega_{pe,i})$ is the electron/ion Debye length, and $Z'(\xi_{e,i})$ is the derivative of the plasma dispersion function

$$Z(\xi_{e,i}) = \frac{1}{\sqrt{\pi}} \int_{-\infty}^{\infty} \frac{e^{-s^2}}{s - \xi_{e,i}} ds$$

(Fried & Conte 2015), where $\xi_{e,i} = \omega/k_\parallel v_{te,i}$.

We are interested in the low beta plasma, and in the kinetic limits, the parallel phase velocity of the wave is greater than the ion thermal velocity but less than the electron thermal velocity, i.e., $\xi_e \ll 1$ (electrons are hot) and $\xi_i \gg 1$ (ions are cold) (Lysak & Lotko 1996). Under the above limits, $Z'(\xi_e) \approx (-2 - 2i\xi_e\sqrt{\pi}e^{-\xi_e^2})$ for electrons and $Z'(\xi_i) \approx (\xi_i^{-2} - 2i\xi_i\sqrt{\pi}e^{-\xi_i^2})$ for ions.

On further simplification by putting $Z'(\xi_e)$ and $Z'(\xi_i)$ in Equation (6) and then employing Equations (5) and (6) in Equation (2), we obtained the real and imaginary parts of ω for KAWs as (Ayaz et al. 2019, 2020)

$$\omega_R = k_\parallel v_A$$
$$\times \left[\frac{\left(1 + \Lambda \frac{15}{4}\right)}{\left(1 + \frac{\Lambda}{4}\right)}\left(1 + \frac{3}{4}k_\perp^2 \rho_i^2\right) + \frac{T_e}{T_i}k_\perp^2 \rho_i^2 \left(1 + \Lambda \frac{15}{4}\right)\right]^{1/2} \qquad (7)$$

and

$$\omega_i = -\Psi k_\parallel v_A,$$

with

$$\Psi = \frac{v_A}{v_{te}} \frac{\left(1 + \Lambda \frac{15}{4}\right)}{2}\left[\frac{T_e}{T_i}k_\perp^2 \rho_i^2 \left\{1 + \left(\frac{T_e}{T_i}\right)^{3/2}\sqrt{\frac{m_i}{m_e}}e^{-\xi_i^2}\right\}\right]\sqrt{\pi}. \qquad (8)$$

Our analytical results (Equations (7) and (8)) are consistent with Khan (2019), who used a kappa-distribution function and

obtained the following relations:

$$\omega_r = k_\parallel v_A \left[\left(1 + \frac{3}{4}\frac{2\kappa}{2\kappa - 3}k_\perp^2 \rho_i^2 \right) + \frac{2\kappa}{2\kappa - 1}\frac{T_e}{T_i}k_\perp^2 \rho_i^2 \right]^{1/2}$$
(9)

and

$$\omega_i = -\gamma k_\parallel v_A,$$

with

$$\gamma = \frac{v_A}{v_{Te}}\left(1 + \frac{2\kappa}{2\kappa - 1}\frac{T_e}{T_i}k_\perp^2 \rho_i^2 \right)^{-1}$$
$$\times \left[\frac{T_e}{T_i}k_\perp^2 \rho_i^2 \frac{2\kappa^2}{(2\kappa - 1)^2}\frac{\sqrt{\pi}}{\kappa^{3/2}}\frac{\Gamma(\kappa + 1)}{\Gamma(\kappa - 1/2)} \right]$$
$$\times \left\{ 1 + \sqrt{\frac{m_i}{m_e}}\left(\frac{T_e}{T_i} \right)^{3/2}\left(1 + \frac{1}{\kappa}\frac{\omega_r^2}{k_\parallel^2 v_{Ti}^2} \right)^{-\kappa - 1} \right\}.$$
(10)

These expressions (Equations (7) and (8)) and their counterparts (Equations (9) and (10)) reduce to the results of Cramer (2011) and Barik et al. (2021, 2023),

$$\omega_i \approx -\sqrt{\frac{\pi}{8}}\frac{k_\perp^2 v_A^2}{\Omega_i^2}\left(\frac{m_e}{m_i} \right)^{1/2}k_\parallel c_s,$$

in the limits $\Lambda = 0$ and $\kappa \to \infty$.

2.2. The Perturbed EM Fields

Making the usual assumption that the perturbed EM fields are in the form of $e^{i(\boldsymbol{k}\cdot\boldsymbol{r} - \omega t)}$ (Lysak 1998), then Faraday's law,

$$\nabla \times \boldsymbol{E} = -\frac{\partial \boldsymbol{B}}{\partial t},$$

translates into

$$\boldsymbol{k} \times \boldsymbol{E} = \omega \boldsymbol{B},$$
(11)

where we have replaced ∇ by $i\boldsymbol{k}$ and $\frac{\partial}{\partial t}$ by $-i\omega$. Because we have assumed that $\boldsymbol{k}$ and $\boldsymbol{E}$ lie in the x–z plane and $\boldsymbol{B}$ is along the y-axis, then according to Equation (11),

$$\frac{E_x}{B_y} = \frac{\omega}{k_\parallel - k_\perp E_z/E_x}.$$
(12)

In Equation (12), we need the ratio E_z/E_x, which we obtained by solving the first row of Equation (2). Thus,

$$\frac{E_z}{E_x} = \frac{k_\parallel^2 c^2 - \omega^2 \epsilon_{xx}}{k_\parallel k_\perp c^2}.$$
(13)

Using Equation (13) in Equation (12) yields

$$\frac{E_x}{B_y} = \frac{c^2 k_\parallel}{\omega \epsilon_{xx}}.$$
(14)

Recalling Equations (5)–(9) and substituting $\omega = \omega_R + i\omega_i$ in Equation (14), we get

$$\frac{E_x}{B_y} = \frac{v_A^2 k_\parallel \left(1 + \Lambda\frac{15}{4} \right)}{\left(1 - \frac{3}{4}k_\perp^2 \rho_i^2 + \frac{\Lambda}{4} \right)}\left[\frac{1}{\omega_R} - i\frac{\omega_i}{\omega_R^2} \right].$$
(15)

The real and imaginary parts in Equation (15) are

$$\mathrm{Re}\left(\frac{E_x}{v_A B_y} \right)$$
$$= \frac{\left(1 + \Lambda\frac{15}{4} \right)}{(1 - \frac{3}{4}k_\perp^2 \rho_i^2 + \frac{\Lambda}{4})\left\{ \left(\frac{1 + \Lambda\frac{15}{4}}{1 + \frac{\Lambda}{4}} \right)\left(1 + \frac{3}{4}k_\perp^2 \rho_i^2 \right) + \frac{T_e}{T_i}k_\perp^2 \rho_i^2 \right\}^{1/2}}$$
(16)

and

$$\mathrm{Im}\left(\frac{E_x}{v_A B_y} \right)$$
$$= \frac{v_A}{2v_{t\parallel e}}\frac{\left(1 + \Lambda\frac{15}{4} \right)\frac{T_e}{T_i}k_\perp^2 \rho_i^2 \{ 1 + \left(\frac{T_e}{T_i} \right)^{3/2}\sqrt{\frac{m_i}{m_e}}e^{-\xi_i^2} \}}{(1 - \frac{3}{4}k_\perp^2 \rho_i^2 + \frac{\Lambda}{4})\left[\frac{1}{1 + \frac{\Lambda}{4}}\left(1 + \frac{3}{4}k_\perp^2 \rho_i^2 \right) + \frac{T_e}{T_i}k_\perp^2 \rho_i^2 \right]}\sqrt{\pi}.$$
(17)

By the same token, Equation (13) can be written as

$$\frac{E_z}{E_x} = \frac{k_\parallel}{k_\perp}\left[1 - \left\{ \left(1 - \frac{3}{4}k_\perp^2 \rho_i^2 + \frac{\Lambda}{4} \right) \right. \right.$$
$$\times \left[\left(1 + \frac{3}{4}k_\perp^2 \rho_i^2 \right) + \frac{T_e}{T_i}k_\perp^2 \rho_i^2\left(1 + \frac{\Lambda}{4} \right) \right]$$
$$- 2i\Psi\left(1 - \frac{3}{4}k_\perp^2 \rho_i^2 + \frac{\Lambda}{4} \right)$$
$$\left. \left. \times \left[\left(1 + \frac{3}{4}k_\perp^2 \rho_i^2 \right) + \frac{T_e}{T_i}k_\perp^2 \rho_i^2\left(1 + \frac{\Lambda}{4} \right) \right]^{1/2} \right\} \right].$$
(18)

After simplifications, the real and imaginary parts in Equation (18) are

$$\frac{k_\perp}{k_\parallel}\mathrm{Re}\frac{E_z}{E_x} = 1 - \left(1 - \frac{3}{4}k_\perp^2 \rho_i^2 + \frac{\Lambda}{4} \right)$$
$$\left[\left(1 + \frac{3}{4}k_\perp^2 \rho_i^2 \right) + \frac{T_e}{T_i}k_\perp^2 \rho_i^2(1 + \frac{\Lambda}{4}) \right]$$

and

$$\frac{k_\perp}{k_\parallel}\mathrm{Im}\frac{E_z}{E_x} = 2\Psi\left(\frac{1 + \frac{\Lambda}{4}}{1 + \Lambda\frac{15}{4}} \right)^{1/2}.$$
(19)

2.3. Poynting Flux Vector of KAWs

The derived EM field ratios, i.e., Equations (12)–(15), are used to find the expression for the Poynting flux vector of KAWs. In general, the steady-state form of the Poynting theorem demands (Lysak & Song 2003) $\nabla \cdot \boldsymbol{S} = -\boldsymbol{P}$, where $\boldsymbol{S}$ is the Poynting flux vector and $\boldsymbol{P}$ is the power dissipation whose real parts are

$$\boldsymbol{S} = \mathrm{Re}(\boldsymbol{E}^* \times \boldsymbol{B})/2\mu_0$$

and

$$\boldsymbol{P} = \mathrm{Re}\,(\boldsymbol{J}^* \cdot \boldsymbol{E})/2,$$

where μ_0 is the permeability constant and $\boldsymbol{J} = \frac{1}{\mu_0}(\nabla \times \boldsymbol{B})$ is the current density.

In our specified geometric configuration (Figure 1), the Poynting vector's y-component (S_y) is naturally null, as the waves exclusively propagate within the x–z plane. We can

write

$$\nabla \cdot \boldsymbol{S} = \frac{\partial}{\partial x} S_x(x,\, z) + \frac{\partial}{\partial z} S_z(x,\, z). \tag{20}$$

In the above Equation (20), the averaged x- and z-components of the Poynting vector are

$$S_z = \mathrm{Re}(E_x^* B_y) \tag{21}$$

and

$$S_x = -S_z\left(\frac{E_z}{E_x}\right), \tag{22}$$

respectively. KAWs having $k_\perp \gg k_\parallel$ can carry some energy across the field lines, but usually that energy is small, employing $S_x \ll S_z$ (Lysak & Song 2003; Khan et al. 2020). Due to their insignificant contributions in certain space environments (plasma sheath, aurora, etc), the x-component, i.e., Equation (22), is not taken into account. In this study, we investigated KAWs in the solar coronal region; however, we are considering both perpendicular and parallel components of Poynting flux (S_x and S_z), as given in Equations (21) and (22).

In the literature, the S_z of KAWs can be written as $S_z = \mathrm{Re}(E_x^* B_y/2\mu_0)$ (Lysak & Song 2003). In this case, the power dissipation expression, employing the parallel components j_z^* and E_z, can be simplified as

$$P = \frac{1}{2} \mathrm{Re}(J_z^* E_z) = k_\perp \, \mathrm{Re}\left(i\frac{E_z}{E_x}\right) S_z = 2\Psi k_\parallel S_z C_0, \tag{23}$$

where we define $C_0 = \left(\frac{1 + \frac{\Lambda}{4}}{1 + 15\frac{\Lambda}{4}}\right)^{1/2}$.

Using the steady-state form of the Poynting flux theorem and ignoring the contribution from S_x, we have

$$\frac{\partial S_z}{\partial z} = -P = 2\Psi k_\parallel S_z C_0, \tag{24}$$

where the solution for S_z is

$$S_z(z) = S_z(0) e^{-2\Psi k_\parallel z C_0}. \tag{25}$$

Here $S_z(0)$ represents the parallel component of the Poynting flux vector at the $z = 0$ location, while the other symbols have their usual meaning. The solution for S_x is then obtained by substituting S_z in Equation (22):

$$S_x(z) = -S_z(0)\left(\frac{E_z}{E_x}\right) e^{-2\Psi k_\parallel z C_0}. \tag{26}$$

Equations (25) and (26) allow us to quantify the conversion of EM energy into thermal energy within the solar flares as the waves propagate spatially from their origin at $z = 0$. Initially, at $z = 0$, where the waves are excited, they possess a Poynting flux of magnitude $S(0)$. As the waves progress, this Poynting flux experiences attenuation. Mathematically, this attenuation arises from a negative ω_i. Physically, it results from wave–particle interactions in which plasma particles extract energy from the waves, causing plasma heating.

3. Results

For the coronal plasma, we have chosen the following parameters: the temperature T is $> 10^6$ K, the density n_0 is
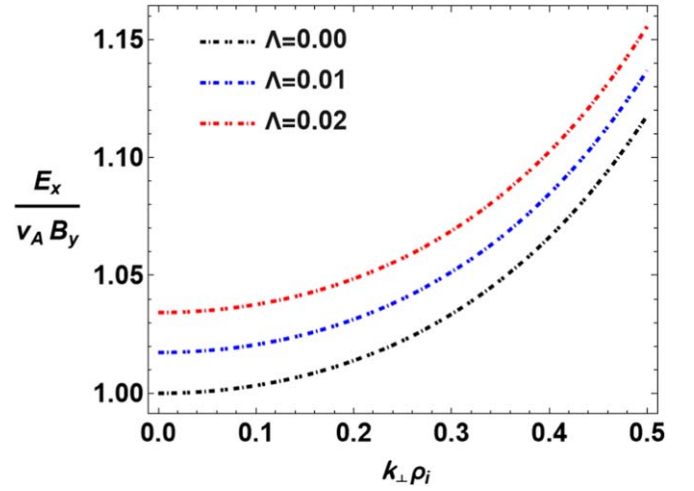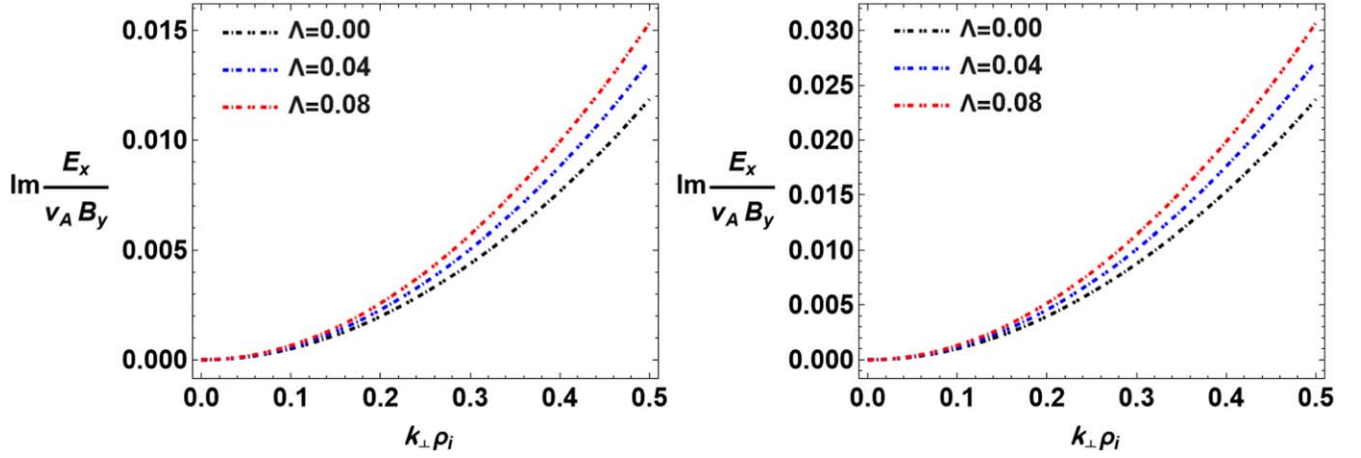

Figure 2. Normalized $E_x/v_A B_y$ vs. $k_\perp \rho_i$ for different values of Λ. The curves are generated based on Equation (16) with a fixed electron-to-ion temperature ratio $T_e/T_i = 0.1$.

10^9–10^{11} cm^{-3}, the magnetic field B_0 is 10–100 G (Zirin 1996; Gary 2001), $k_\perp/k_\parallel \sim 100$–115 (Chen & Wu 2012; Singh & Jatav 2019), and the plasma beta is $\beta_p = 4\pi n_0 T/B_0^2 = 3.6 \times 10^{-3} \ll 1$ (for $B_0 = 50$ G, $n = 10^9$ cm^{-3}, $T = 10^6$ K).

We discern a noteworthy dependence of the nonthermal parameter ($\Lambda \geqslant 0$) on the normalized EM field ($E_x/v_A B_y$) of KAWs (Figure 2) . Notably, in contrast to a Maxwellian plasma (i.e., $\Lambda = 0$), the ratio of the normalized $E_x/v_A B_y$ exhibits a conspicuous rise with increasing values of both Λ and the perpendicular wavenumber ($k_\perp \rho_i$). These variations in the EM field concerning Λ and $k_\perp \rho_i$ corroborate the recent observations presented in Lysak (2023). As anticipated from Equation (16), this field ratio approaches unity for relatively small $k_\perp \rho_i$, subsequently increasing $k_\perp \rho_i$ is in agreement with the wave's transition toward an electrostatic character. An important observation is that a wide spectrum of Λ values within the nonthermal regime can capture intricate details of the EM field fluctuations. These fluctuations have been routinely documented in space plasmas (Wygant et al. 2002; Khan et al. 2020). Consequently, notwithstanding alternative factors such as gyroradius correction terms, the nonthermal nature of the system emerges as a significant contributor to the dynamics of the EM field within KAWs. Intriguingly, we extend our investigation to examine the impact of the imaginary part of the normalized perturbed field $\mathrm{Im}(E_x/v_A B_y)$ ratio on the wave profile. As depicted in Figure 3, we discern that the magnitude of $\mathrm{Im}(E_x/v_A B_y)$ experiences augmentation for $\Lambda > 0$. While this aspect has often been overlooked due to its perceived small contribution, our inclusion of it stems from our focus on studying KAWs within the context of solar coronal regimes. The extent of this contribution's smallness has remained undetermined. We have addressed this analytically, as is evident in Equation (17) and Figure 3, which illustrate the amplification of imaginary EM field perturbations with increasing Λ values.

Additionally, we see that the $\mathrm{Im}(E_x/v_A B_y)$ is also influenced by different magnetic field $\boldsymbol{B}$ values. In the strong $\boldsymbol{B}$ field of 100 G (i.e., the right panel), the magnitude of $\mathrm{Im}(E_x/v_A B_y)$ is increased compared to the weak $\boldsymbol{B}$ of 50 G (left panel). The increase/decrease in the magnitude of the imaginary perturbed EM field of KAWs in the solar corona under a strong and weak magnetic field carries significant physical implications. The

Figure 3. Dependence of the normalized imaginary field $\mathrm{Im}(E_x/v_A B_y)$ on $k_\perp \rho_i$ for different values of Λ. The plots are based on Equation (17) with the following parameter values: $v_{te} = 1.34 \times 10^9$ cm s^{-1}, $v_{ti} = 1.95 \times 10^7$ cm s^{-1}, and $T_e/T_i = 0.5$. We have assumed $\boldsymbol{B} = 50$ G in the left panel and $\boldsymbol{B} = 100$ G in the right panel to see how the magnetic field affects the magnitude of $\mathrm{Im}(E_x/v_A B_y)$.
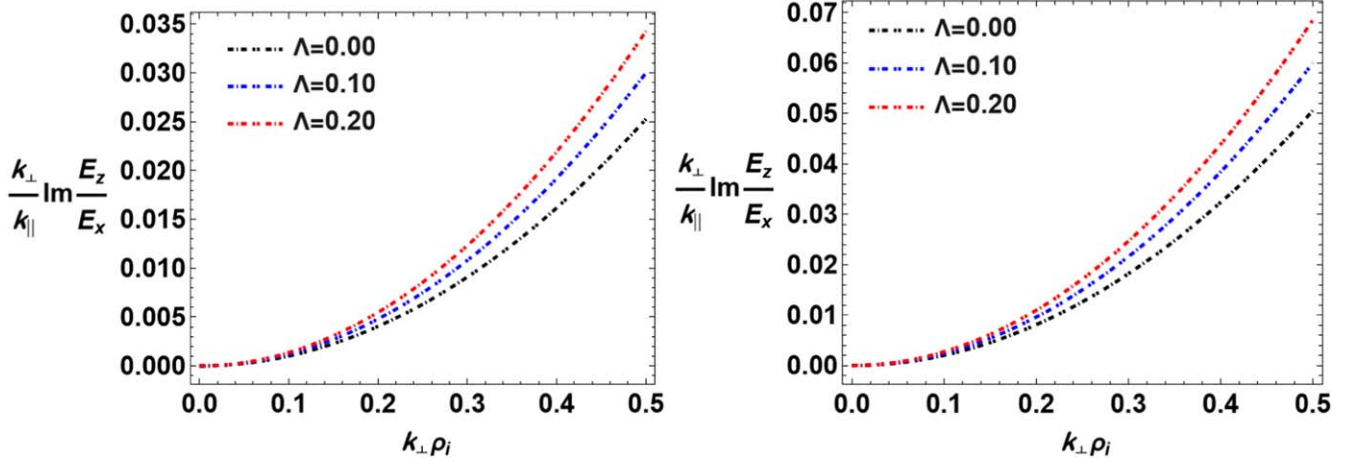

Figure 4. Variation of imaginary $k_\perp/k_\parallel \, \mathrm{Im}(E_z/E_x)$ vs. $k_\perp \rho_i$ for different Λ. The curves are plotted using Equation (19) with the same parameter values that we used in Figure 3. In both cases, when (left panel) $\boldsymbol{B} = 50$ G and (right panel) $\boldsymbol{B} = 100$ G, the normalized field ratio is enhanced for $\Lambda > 0$.

strength of the magnetic field directly influences the characteristics and behavior of the wave, such as wave propagation, wave–particle interactions, and energy transfer processes within the plasma environment. In a strong magnetic field scenario, the plasma exerts a greater influence on the motion of charged particles and enhances wave–particle interactions, thus causing more pronounced perturbations in the EM field. This leads to an increase in the magnitude of the perturbed EM field ratio of KAWs. This suggests that the energy associated with the KAWs can be transported quickly over the distance. Conversely, in regions where the magnetic field is weaker, the influence on particle motion is reduced, resulting in lesser perturbations and a decrease in the magnitude of the perturbed field ratio. Therefore, the observed variation in the perturbed EM field ratio with changes in the magnetic field strength reflects the intricate interplay between wave dynamics and plasma properties. In the work of Duckenfield et al. (2021), the influence of $\boldsymbol{B}$-field strength on the wave phenomena in the solar corona is explored. It is presented that the direct relationship between magnetic field strength effectively affects the wave damping rate.

Looking at Equation (17), we see that the imaginary part of the EM field ratio remains relatively small compared to the real part for our chosen parameters. Prior studies by Lysak (1998),

Lysak & Song (2003), Khan et al. (2019), and Khan (2019) primarily focused on wave dynamics outside the solar corona, overlooking these subtle contributions. In contrast, our investigation of the solar corona, particularly in warm plasma scenarios, underscores the significance of even minor contributions. Drawing upon the work of Lysak & Song (2003), we acknowledge that the $E_x/v_A B_y$ ratio's small imaginary part may appear inconsequential in the nearby Sun's environment. However, our meticulous analysis, especially of the Poynting flux expressions, reveals a different narrative. We find that KAWs exhibit pronounced damping for higher values of the index Λ, compelling us to account for these nuanced influences. This observation explicitly finds resonance in Polar observations by Wygant et al. (2002), which provide empirical evidence of the ion gyroradius effect amplifying the E_x/B_y ratio. Understanding these effects assumes critical importance in elucidating phenomena within space plasmas and astrophysical environments. Furthermore, these results offer insights into the role of field-aligned currents in solar flares, shedding new light on this phenomenon.

Likewise, $E_x/v_A B_y$, the imaginary part of the normalized $k_\perp E_z/k_\parallel E_x$, is enhanced for different values of Λ and $k_\perp \rho_i$ (Figure 4). When $k_\perp \rho_i$ increases, for large values of Λ, the $k_\perp/k_\parallel \, \mathrm{Im}(E_z/E_x)$ rises gradually as compared to the Maxwellian
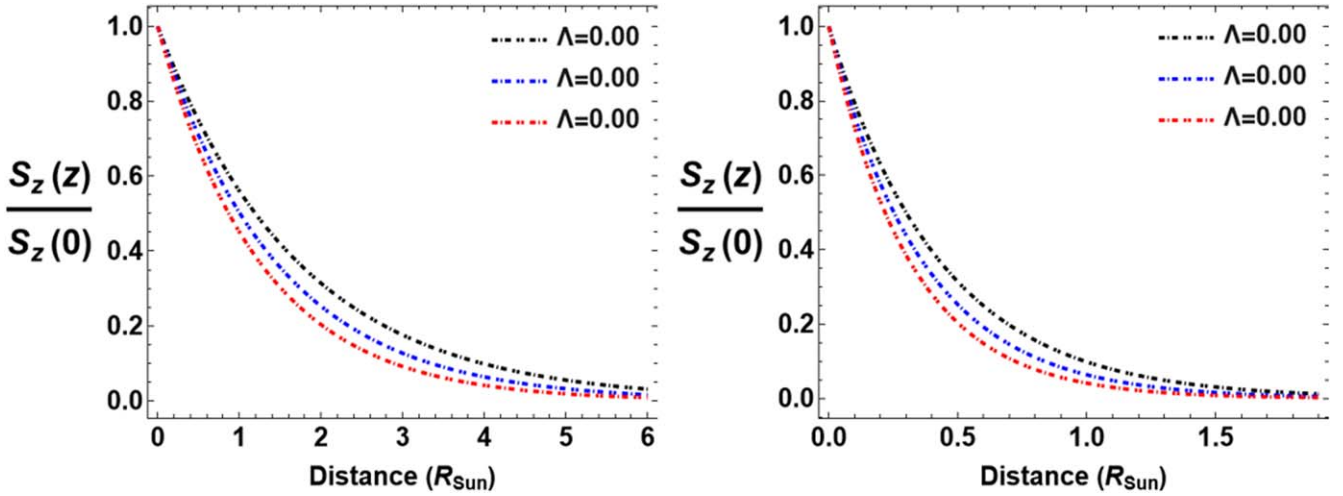
Figure 5. The normalized Poynting flux $S_z(z)/S_z(0)$ vs. distance R_{Sun} (which is in units of the Sun's radius) for different values of Λ. We assumed $\rho_i \approx 82$ cm, $k_\perp = 1.8 \times 10^{-4}$ cm^{-1}, $h = 0.1\ R_{Sun}$, and $k_\parallel = 1.8 \times 10^{-6}$ cm^{-1}, and the other parameters are the same as in Figure 3. In the left panel, $B = 50$ G, and in the right panel, $B = 100$ G. The Poynting flux decays rapidly when either B or Λ increases.

distributed plasma. We also see that the magnitude of $k_\perp/k_\parallel\ \mathrm{Im}(E_z/E_x)$ is smaller than $E_x/v_A B_y$ and larger than $\mathrm{Im}(E_x/v_A B_y)$ for a given $k_\perp\rho_i$ values (Figures 2, 3, and 4). It is shown that the difference between Maxwellian and suprathermal regimes becomes prominent for larger values of $k_\perp\rho_i$. This amplification in $k_\perp/k_\parallel\ \mathrm{Im}(E_z/E_x)$ with $k_\perp\rho_i$ and Λ in KAWs within the solar corona denotes a noteworthy correlation between multiple plasma parameters and wave dynamics. This signifies a heightened sensitivity of the electric field components to variations in $k_\perp\rho_i$ and Λ, suggesting potential alterations in wave polarization. Such amplification implies a more intricate and possibly unstable behavior in wave characteristics, likely influencing energy dissipation or modifying the energy transfer pathways in the corona.

In general, if the amplitude of the parallel electric field is large enough to accelerate electrons to velocities above thermal velocity, or even up to Alfvén velocity ($v_{te} < v_A$ for low β_p), the particle distribution becomes unstable. This unstable distribution shifts the resonant particles participating in the wave–particle interactions, thus making KAWs unstable. This unstable KAW can grow and play an important role in the energy transport in solar coronal plasma. Even though there are minimal variations in the nonthermal particles Λ, the wave becomes significantly unstable and can carry a large amount of energy in the solar corona. The EM energies of the damped/unstable waves are converted into heat energy as the waves travel across. As shown in Equation (19), the imaginary part of E_z/E_x is directly related to the Landau damping rate Ψ, which results from the resonance condition $\omega = k_\parallel v_\parallel$. In the case of KAWs, the ion dynamics shifts the resonance point toward the tail of the electron distribution (Lysak & Lotko 1996). And, in the tail, the resonant particles are large even for small values of Λ, which means that the small values of Λ should increase the magnitude of the imaginary part of the electric field E_z/E_x ratio for a given $k_\perp\rho_i$.

Studies such as Khan et al. (2020) delve into nonthermal effects, i.e., kappa (κ), and plasma parameter influence on solar coronal wave dynamics affirming the observed changes in $k_\perp/k_\parallel\ \mathrm{Im}(E_z/E_x)$ in response to variations in $k_\perp\rho_i$ and Λ. These investigations highlight the intricate relationship between $k_\perp\rho_i$, Λ, and the electric field components (E_x and E_z) in KAWs,

underscoring their pivotal role in comprehending wave behavior within the solar corona's dynamics.

In Figure 5, we see that the normalized Poynting flux $S_z(z)/S_z(0)$ falls off rapidly for larger values of Λ. As mentioned earlier, the electric and magnetic fields of KAWs carry EM energy stored in them; the question is how the transfer occurs spatially when the waves move forward. This information is contained in $S_z(z)/S_z(0)$, which explicitly depends on spatial coordinate z. It is obvious from Figures 5 that the Poynting flux decays rapidly for large values of Λ and gradually for small values of Λ. All this is due to the Landau mechanism. For large Λ, the EM energy of the wave is converted to Landau resonant electrons, which dissipate the wave quickly, thus accelerating the particle over a short distance. This should be the case because, in the large Λ situation, the energy is distributed over a large number of nonthermal particles, which causes the wave to run out of energy quickly. On the other hand, when the magnetic field is changed (i.e., 100 G; the right panel), the dissipation trends of the Poynting flux remain the same, but the distance over which the wave transporting energy is significantly changed. Now the waves transport the energy over a short distance (R_{Sun}) as compared to its counterpart when $B = 50$ G for the same variations in Λ and the other parameters. This implies that in the strong B, the Poynting flux decays rapidly, making the wave completely deliver its energy within a short distance.

As we have discussed, the Poynting flux decays at a relatively fast rate in the case of a strong magnetic field, and a notable disparity arises in the distance (R_{Sun}) over which the wave transports energy under each scenario. In a weak magnetic field, the wave exhibits a remarkable capacity for energy transportation over an extensive distance, contrasting with its behavior in a strong magnetic field. This discrepancy aligns with our expectations, given that the stronger magnetic field accelerates the wave's damping rate within the solar flux tube loop, thereby limiting its travel distance. This observation is corroborated by Duckenfield et al. (2021), underscoring the direct relationship between magnetic field strength and damping effects. Moreover, the difference between Cairns and Maxwellian becomes the same for a relatively larger distance R_{Sun}. One might expect that the wave lingers on for a
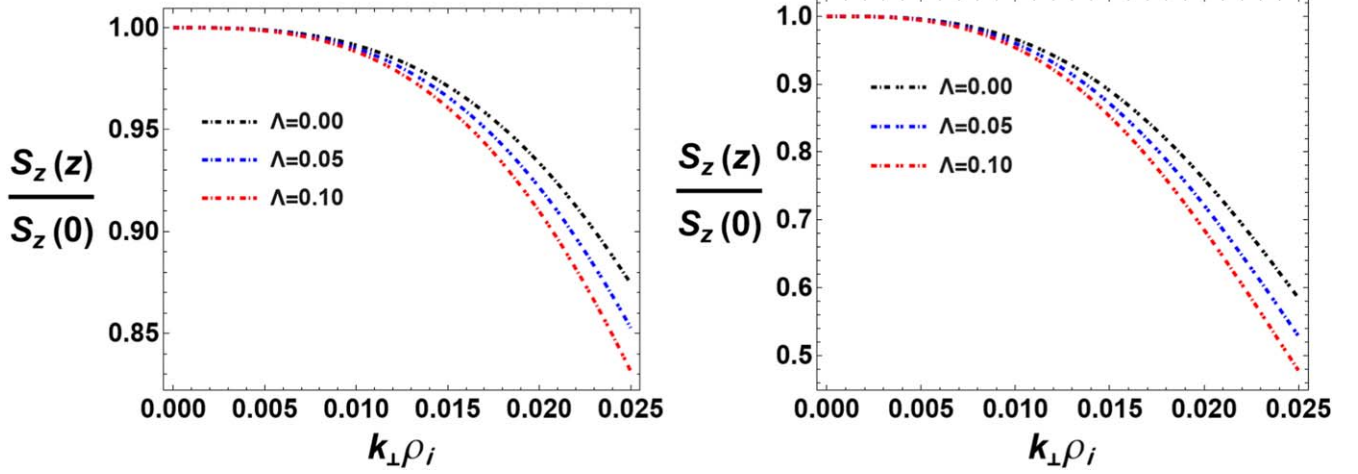
Figure 6. The normalized Poynting flux $S_z(z)/S_z(0)$ vs. $k_\perp\rho_i$ for different values of Λ. We assumed $h = 0.05\ R_{Sun}$, and the other parameters are the same as in Figure 5. In the left panel, $B = 50$ G, and in the right panel, $B = 100$ G.
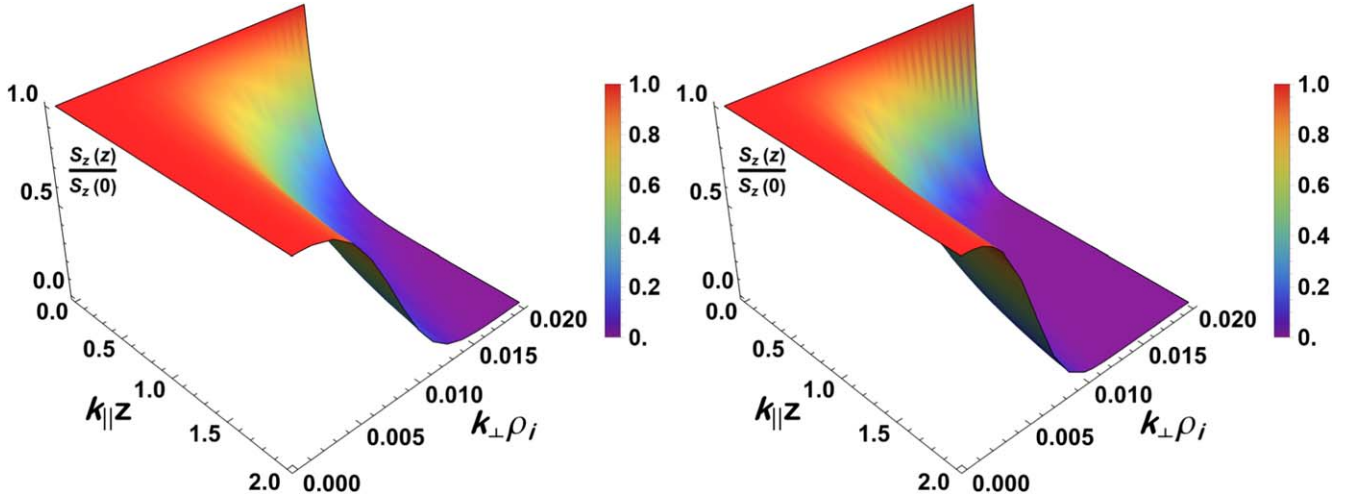
Figure 7. The normalized Poynting flux $S_z(z)/S_z(0)$ as a function of normalized distance $k_\parallel z$ and $k_\perp\rho_i$. The 3D plots are generated using Equation (25) with the same parameter values used in Figure 3. The color sidebar legends to the right show the corresponding values of the normalized Poynting flux of KAWs. In the left panel, $\Lambda = 0$ (i.e., Maxwellian), and in the right panel, $\Lambda = 0.5$ (Cairns).

large number of nonthermal particles Λ, and a larger magnetic field B can transport its energy faster over the distance. If the nonthermality of the system affects the transport of energy—which seems to be the case—then these results can play an important role in the space plasmas.

Besides the variation of Poynting flux versus distance R_{Sun}, we also evaluated $S_z(z)/S_z(0)$ versus $k_\perp\rho_i$ for different values of Λ as shown in Figure 6. We see that the Poynting flux dissipates rapidly for $\Lambda \geqslant 0$ in the case of the strong magnetic field (right panel). Furthermore, the difference in the curves is visible only for moderate values of $k_\perp\rho_i$. This observation is consistent with Khan & Murtaza (2018), Khan (2019), and Khan et al. (2020), where they show that at different values of the perpendicular wavenumber $k_\perp\rho_i$, a larger wave Poynting flux is speculated to produce acceleration over a moderate range of distance. This investigation is also presented in Shukla et al. (2009). Moreover, Wygant et al. (2002) found that Alfvénic Poynting flux is an important energy transfer mechanism throughout the space plasmas.

In the 3D case, the normalized parallel Poynting flux $S_z(z)/S_z(0)$ is significantly affected by both $k_\perp\rho_i$ and the normalized distance $k_\parallel z$. Compared to Maxwellian (Figure 7, left panel), the Poynting flux of KAWs having large perpendicular wavenumbers decays at a faster rate with distance when $\Lambda > 0$ (Figure 7, right panel). As the wave propagates from one place to another, it decays rapidly based on the wave–particle interactions (i.e., resonance conditions) discussed in detail in the discussion section.

Figure 8 presents a depiction of the normalized perpendicular Poynting flux $S_x(z)/S_z(0)$ of KAWs with varying values of Λ. Notably, it becomes evident that S_x exhibits a moderate decay when compared to its counterpart, S_z, particularly for $\Lambda > 0$. The rationale behind this phenomenon lies in the perpendicular component of the EM field associated with KAWs, which is understood to carry energy along the field lines at relatively lower rates, particularly in the limit where $k_\perp > k_\parallel$. The density inside and outside of the flux tube loop is generally different. The width of the tube loop is small compared to its height. We suggest that the width of the tube loop might be determined by the S_x component of the Poynting flux vector. This component is the one making a full semicircle loop. Due to its small contribution, this part (S_x) is usually not considered in the existing literature.
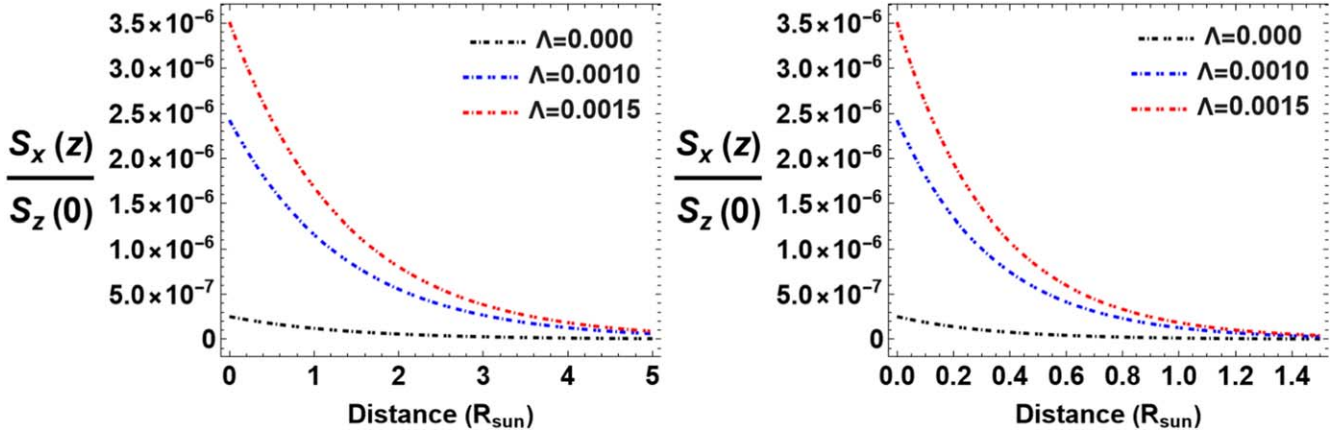
Figure 8. Variation of the normalized perpendicular Poynting flux ($S_x(z)/S_z(0)$) vs. distance (R_{Sun}) for different values of Λ. The curves are based on Equation (26) with the same parameter values used in Figure 3. In the left panel, we assumed $\mathbf{B} = 50$ G, and in the right panel, $\mathbf{B} = 100$ G. We see that the perpendicular Poynting flux is significantly affected by both Λ and magnetic field $\mathbf{B}$.
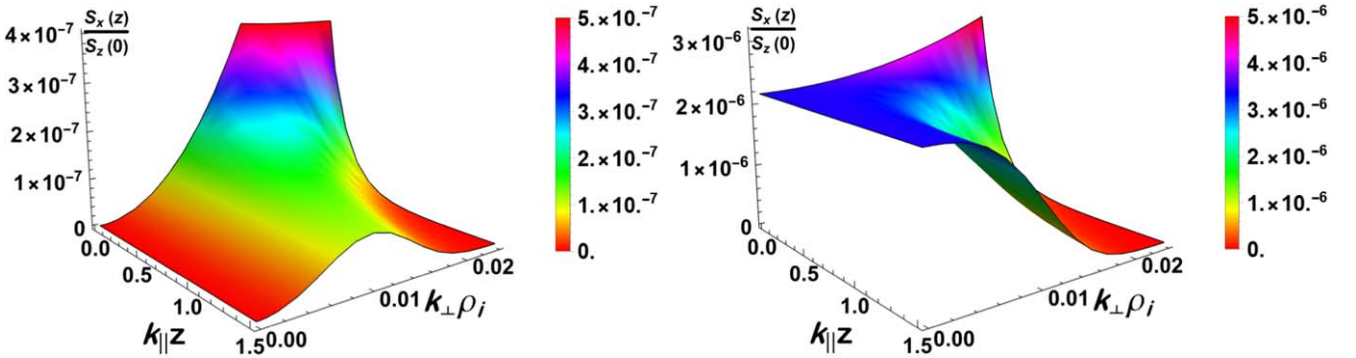
Figure 9. The perpendicular Poynting flux $S_x(z)/S_z(0)$ of KAWs as a function of normalized distance $k_\parallel z$ and $k_\perp \rho_i$. The plots are generated based on Equation (26) with the same parameter values used in Figure 3. The color sidebar legends to the right show the corresponding values of the normalized Poynting flux. The left panel represents the Maxwellian case, i.e., $\Lambda = 0$, and the right panel represents Cairns distributed situations when $\Lambda = 0.5$.

In this study, we have addressed this gap through mathematical calculations (see Equation (26)), the results of which are visually presented in Figures 8 and 9, offering insight into the magnitude of this effect. A second plausible explanation for this observation is the relatively weaker wave–particle interactions occurring in the perpendicular directions and also the strong $\mathbf{B}$ field inside the tube loop. The perpendicular component S_x gives information about the energy transfer along the width of the flux tube. In comparison to the normalized S_z, we see that the perpendicular flux (S_x) dissipates rapidly even before reaching $h = 1.5$ R_{Sun} (i.e., Figure 8, right panel). In our specific geometry (Figure 1), the electric field also contributes to the perpendicular Poynting flux S_x together with the strong magnetic field; for instance, see Equation (26). In the strong magnetic field regions, the Alfvén speed increases, changing the resonance condition. In that direction, the wave interacts with more resonant particles over short distances, causing it to lose its energy rapidly. Our research emphasis was thus centered on precisely quantifying this aspect, which had remained unexplored within the existing body of knowledge.

4. Discussion

Our research reveals that the perturbed EM fields and the Poynting flux of KAWs experience notable alterations within Cairns distributed plasmas. Compared to Maxwellian plasma,

our findings demonstrate that the electric and magnetic field perturbations exhibit greater magnitudes in high-energy environments characterized by large values of Λ. Additionally, we observe a moderate decay rate in the resulting parallel and perpendicular Poynting fluxes. These results hold across a wide range of Λ and $k_\perp \rho_i$ values, providing insights into the fluctuations of these two quantities. Such fluctuations based on these parameters have been consistently observed and supported by spacecraft observations (Khan & Murtaza 2018; Khan 2019; Khan et al. 2020 and references therein). Analysis of data obtained from the Polar spacecraft (Wygant et al. 2002) reveals frequent deviations of E_x/B_y from Alfvénic speed v_A. The possibility of this deviation, specifically in the Maxwellian distribution, can be attributed to the nonnegligible correction factor $k_\perp \rho_i$. Our findings take a step further by proposing an alternative possibility. We propose that the presence of the inevitable spectral index Λ, even with a fixed $k_\perp \rho_i$, adequately explains the departure of E_x/B_y from v_A.

The variations in the imaginary part of E_z/E_x in KAWs depend on the nonthermal index Λ and $k_\perp \rho_i$. This situation can be attributed to the involvement of resonant particles in wave–particle interactions. During the resonance condition ($\omega = k_\parallel v_\parallel$), the nonthermal particles, characterized by the index Λ, significantly influence the energy transfer of KAWs in the form of heat in the coronal plasma. In the designated distribution function, the parameter Λ changes the number of

resonant particles. As mentioned earlier, the resonant points are shifted toward the electron distribution tail due to the ions' dynamics. According to Equation (19), the imaginary part arises from the resonance condition when particles in the distribution possess the same velocity as the phase velocity of KAW (i.e., $\omega/k_\parallel = v_\parallel$). In the case of KAWs, the phase velocity of the wave is lower than the thermal velocity ($\omega/k_\parallel < v_{te}$). In the Cairns distribution, it becomes evident that there is a greater abundance of resonant particles for larger values of Λ, indicating that higher values of Λ are likely to amplify the magnitude of $\mathrm{Im}(E_z/E_x)$ for a given $k_\perp \rho_i$. More detailed information on the significant role played by nonthermal particles in the resonance condition is given in the recent work of Barik et al. (2021).

In the expressions for the Poynting flux, it becomes evident that the wave converts its EM energy to the Landau resonant electrons, presenting numerous possibilities based on different states indicated by the index Λ. In the nonthermal plasmas, as opposed to Maxwellian plasmas, the wave exhibits a more extensive conversion of EM energy to the Landau resonant electrons across significant distances. This outcome is expected since, in the regime of large Λ, the energy is distributed among a larger population of resonant particles, resulting in a faster decay of the wave. Consequently, higher values of Λ prove advantageous for heating or accelerating plasma particles over long distances, a phenomenon that could potentially be observed in the solar flares, solar wind, and plasma sheet boundary layer.

In this extensive investigation, we also incorporated the effects of the perpendicular electric field and the associated Poynting flux vector S_x. While it is common practice to disregard these contributions due to their apparent insignificance, their exact magnitude has remained unclear. However, our study delves into the behavior of KAWs in the context of solar flares, where even these seemingly minor contributions play a crucial role, potentially shaping the loop structures observed. Notably, within the tube loop, the parallel component of S_z holds significant importance, while the perpendicular component S_x primarily influences the energy transfer along the loop's width. As depicted in Figure 8, our findings offer a clear estimate of the magnitude of this perpendicular contribution, shedding light on its actual significance.

In addition to our previous analyses, we delved into the comprehensive examination of the total power transfer rate that comes out and propagates across the flux tube loop. This information might be explained by both the parallel S_z and perpendicular S_x components of the Poynting flux vector. In this situation, we substitute $z = h\theta$ in Equation (26) and then integrate the angle θ from 0–$\pi/2$ to get

$$\frac{S_x(z)}{S_z(0)} = I_x = a\left(\frac{E_z}{E_x}\right)\left(\frac{-1 + e^{-\Psi k_\parallel C_0 h\pi}}{\Psi k_\parallel C_0}\right)\pi. \qquad (27)$$

In the above equation, h is height and a is the radius of the cross section of the flux tube, which we assumed to be circular as shown in Figure 1 (right panel). Similarly, Equation (25) gives

$$I_z = a^2 (e^{-\Psi k_\parallel C_0 h\pi})\pi. \qquad (28)$$

Equations (27) and (28) elucidate the computation of power rates concerning I_x and I_z of KAWs within flux loop tubes. This further gives the total estimate of the flux coming out of the tube loop:

$$\frac{I_x}{I_z} = -\left(\frac{E_z}{E_x}\right)\left(\frac{1 - e^{-\Psi k_\parallel C_0 h\pi}}{a\Psi k_\parallel C_0 e^{-\Psi k_\parallel C_0 h\pi}}\right). \qquad (29)$$

Following Li et al. (2023), we take a to be in the range (700–7000) km. In Effenberger et al. (2017), the height for 61 occult flare loops was examined. We follow that study and assume a (0.05–0.1) R_{Sun} range for h. The same range of h was considered in Li et al. (2023) to examine solar energetic neutral particles. The comprehension of the aggregate energy transfer rate is pivotal for gauging the extent of energy conveyance by these elements within the loop configurations, vividly illustrated in Figures (10) and (11). Notably, we discern a substantial augmentation in the power delivery rate, I_x/I_z, with the variations of the perpendicular wavenumber $k_\perp \rho_i$ at fixed $h = 0.1$ R_{Sun}; see Figure 10 (left panel). We observed that for minor increments in the values of $k_\perp \rho_i$, the magnitude of the power transfer rate in the tube loop is significantly enhanced. In the context of KAWs in the solar corona, this phenomenon suggests that small changes in the $k_\perp \rho_i$ can lead to substantial alterations in the efficiency and intensity of energy transfer processes within the flux tube. Specifically, as $k_\perp \rho_i$ increases, the power transfer rate experiences a pronounced enhancement in the magnitude. Physically, this indicates that KAWs with slightly higher perpendicular wavenumbers are more effective at transporting energy along the flux tube, and they do so at a faster rate. This heightened power transfer capability implies a greater ability to propagate energy over larger spatial scales within the solar corona. As a result, the waves can efficiently transport energy and momentum outside the confinement region, thus indicating how the wave transports power in a flux tube loop. Consequently, this points to the capability of KAWs to effectuate plasma particle heating over extended distances, which holds profound implications for their role in heliophysics.

In the proceedings analysis, we considered $h = 0.1$ R_{Sun} (~35 Mm); however, upon reducing h to $h = 0.05$ R_{Sun}, we see that the power rate I_x/I_z is significantly affected as shown in Figure 10 (right panel). This time, the magnitude of the power rate is reduced, and the wave delivers energy at a moderately slower rate. The power transfer rate of KAWs in the solar flux tube loops reveals a significant height dependence. At a height of $h = 0.1$ R_{Sun}, the power transfer rate is markedly enhanced across various normalized wavenumbers, suggesting optimal resonance conditions, stronger density, magnetic field gradients, and efficient wave–particle interactions conducive to energy transfer. On the other hand, at $h = 0.05$ R_{Sun}, the power transfer rate is significantly reduced, likely due to weaker resonance conditions, lower plasma density, and diminished magnetic field strength, which collectively impede the efficient transfer of energy. These findings underscore the sensitivity of KAW energy transfer to local plasma conditions and magnetic field structures that are crucial for understanding coronal heating and solar wind acceleration.

In general, the values of $k_\perp \rho_i$ directly influence the power transfer rate of KAWs. Inside the flux loop tube, the magnetic field strength is strong enough to make the wave deliver power quickly for the given $k_\perp \rho_i$. The impact can be elucidated through the examination of large and small $k_\perp \rho_i$ that contribute to and affect the power rate of KAWs. In case of large $k_\perp \rho_i$, KAWs exhibit characteristics distinct from shorter $k_\perp \rho_i$. In realistic observations, Alfvén velocity v_A is higher in larger $k_\perp \rho_i$, implying that Alfvén waves can propagate power more rapidly. This can contribute to a decrease in the magnitude of
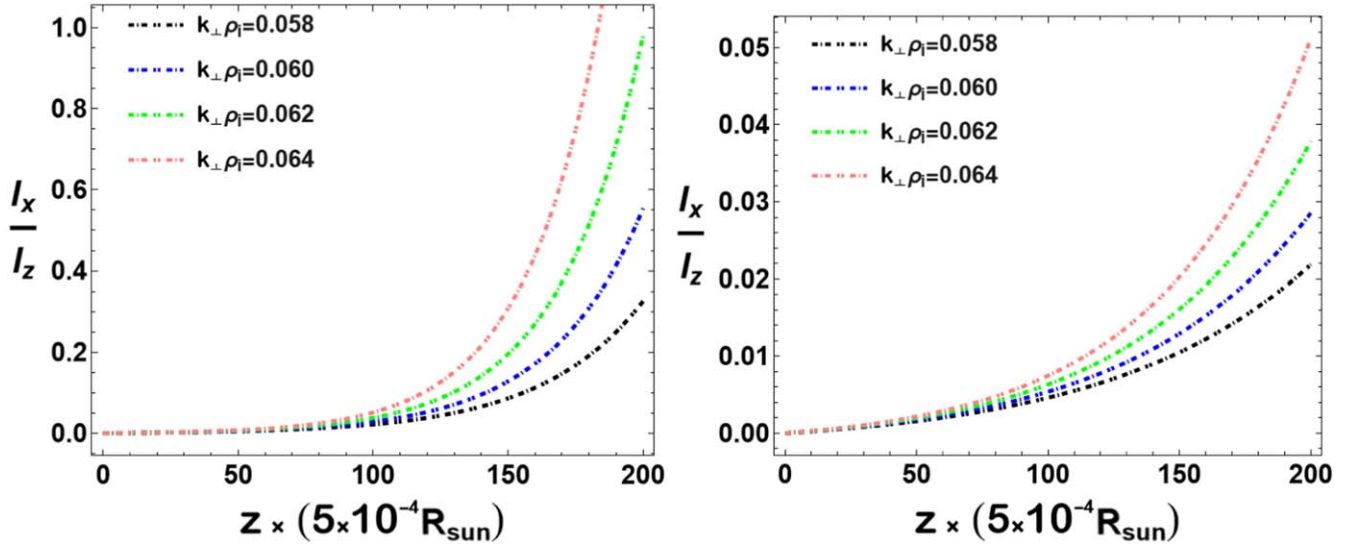
Figure 10. Variation of I_x/I_z vs. normalized distance $z \times (0.0005) \, R_{Sun}$ for different values of $k_\perp \rho_i$. The parameters $\boldsymbol{B} = 50$ G, $a = 7 \times 10^7$ cm, $k_\perp \approx 8.5 \times 10^{-4}$ cm^{-1}, $k_\parallel \approx 8.5 \times 10^{-6}$ cm^{-1}, and $\Lambda = 0$ are kept constant. In the left panel, $h = 0.1 \, R_{Sun}$, and in the right panel, $h = 0.05 \, R_{Sun}$.
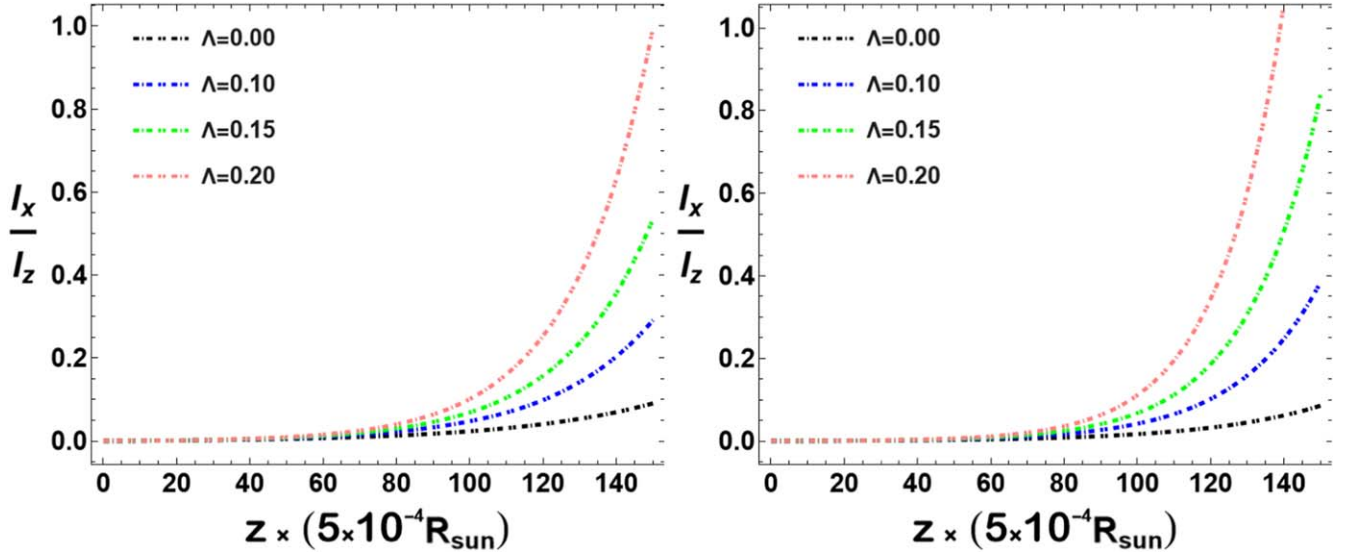
Figure 11. Variation of I_x/I_z vs. $z \times (0.0005) \, R_{Sun}$ for different values of Λ. The other values are the same as we used in Figure 10. In the left panel, $\boldsymbol{B} = 50$ G, and in the right panel, $\boldsymbol{B} = 100$ G.

the power rate for certain wave modes. Large $k_\perp \rho_i$ often leads to higher frequencies of the waves. In contrast, short $k_\perp \rho_i$ results in lower v_A and slower wave propagation. The power rate of KAWs is reduced in shorter $k_\perp \rho_i$ because the wave interacts with particles and is quickly damped out. Thus, the magnitude of the power rate increases.

In the above situations, we evaluated I_x/I_z for different values of $k_\perp \rho_i$ and h, where we assumed $\Lambda = 0$ (i.e., KAWs in the Maxwellian distributed plasma). Our main focus is the effect of the nonthermal particles Λ on the wave dynamics as shown in Figure 11. We see that the magnitude of I_x/I_z is significantly enhanced for $\Lambda > 0$, which gives information as to how the wave–particle interaction occurs in the flux tube loop. It is obvious from the figures that Λ plays a crucial role in the flux rate coming out of the tube loop and propagating in the tube. Both the left and right panels of Figure 11 are plotted for fixed $\boldsymbol{B} = 50$ G and $\boldsymbol{B} = 100$ G with $k_\perp \rho_i \approx 0.05$ and $k_\perp \rho_i \approx 0.04$, respectively. We observe that

the power delivery rate is more prominent at a larger normalized distance R_{Sun}. Compared to the more common Maxwellian distribution (i.e., the black curves), the Cairns distributed KAWs exhibit a notably faster power transfer rate for larger values of Λ. The waves transport power quickly, suggesting that, in regions like the solar corona, KAWs are more efficient in transporting greater amounts of energy over distance beyond the confines of the flux tube. The phenomenon can be attributed to the unique characteristics of the Cairns distribution, where a higher Λ indicates an increased population of nonthermal particles with higher kinetic energies. These nonthermal particles interact with the waves, leading to enhanced wave–particle resonance and energy transfer, allowing for more effective energy transport processes.

From all these discussions, we observed that our investigations unveiled a noteworthy effect of the nonthermal parameter Λ, the perpendicular wavenumber $k_\perp \rho_i$, the $\boldsymbol{B}$-field effect, and the different height h, resulting in a substantial influence in the power

rate of KAWs in the solar atmosphere. Of particular importance is the investigation of the perturbed electric and magnetic fields for the analysis of KAWs because spacecraft, as shown by observations (Wygant et al. 2000, 2002; Keiling et al. 2002; Lysak & Song 2003; Smith et al. 2011 and references therein), have measured them directly, rather than determining the damping rate, which further extended to the Poynting flux and power delivery rate of KAWs. Our results suggest that higher values of Λ, in comparison to a Maxwellian distribution, enhance the effectiveness of energy transport by KAWs over extended distances. These insights hold promise for understanding regular fluctuations in EM field perturbations, the Poynting flux, and the power deliver rate in various space plasma environments.

The findings of the present work underscore the heightened efficiency of KAWs in heating and accelerating nonthermal particles within the plasma. Such findings hold significant implications for our comprehension of plasma behavior in a diverse range of astrophysical and laboratory contexts (Cramer 2011; Wu & Chen 2020). They can be applied to various space environments where KAWs, characterized by non-Maxwellian distributions, are prevalent.

5. Conclusion

In summary, our findings reveal the significant influence of nonthermal particles, represented by the Cairns distribution with parameter Λ, on the perturbations of EM fields, the Poynting flux vector in the parallel and perpendicular directions, and the total power transfer rate of KAWs. The analysis is centered on the phenomena of the perturbed EM fields. We found that the real and imaginary normalized EM fields, $\mathrm{Re}(E_x/v_A B_y)$ and $\mathrm{Im}(E_x/v_A B_y)$, are significantly influenced by nonthermal particles Λ. We also evaluated $\mathrm{Im}(E_z/E_x)$, which plays a crucial role in wave–particle interactions for different values of Λ. These fluctuating EM fields of KAWs are responsible for transporting the EM energy stored in them. Specifically, our investigation into estimating the perpendicular Poynting flux vector and power delivery of KAWs uncovered fascinating phenomena, demonstrating their efficient energy transport through and out of the tube loops. We found that the KAWs are dissipating at a faster rate for $\Lambda > 0$. Moreover, the evaluation of the power rate for different parameters (Λ, $\boldsymbol{B}$, $k_\perp \rho_i$, and h) gives detailed information about the heating phenomena of KAW in the solar flux tube loop. We found that the magnitude of the power delivered by KAWs is significantly influenced. The analytical findings will find potential applications in heliospheric physics, where nonthermal particles characterized by nonthermal index parameters are often observed.

The current study is primarily centered on the isotropic behavior of particles (electrons and ions), characterized by the isotropic Cairns distribution. Future research endeavors should systematically explore scenarios involving temperature anisotropy to broaden the scope of our findings. The distinct behaviors exhibited by particles in parallel and perpendicular directions present an intriguing avenue for inquiry. Future research will uncover how temperature anisotropy modulates the dynamics of KAWs and their wave–particle interactions in the solar corona. Furthermore, extending our inquiry to encompass the estimation of the resonant velocity and the characteristic damping length of KAWs holds significant promise. These estimations contribute to gauging the distance the particles traverse, imparting energy to the wave, and providing valuable insights into the spatial extent over which the wave dissipates. Moreover, future investigations could delve into the intricate realms of density inhomogeneity

and instability or the combination thereof. Incorporating these aspects as extensions of the present work would provide a more comprehensive understanding of the complex interplay between plasma properties and KAW dynamics. These extensions promise to advance our knowledge of KAWs in solar coronal plasmas, paving the way for a more complete and nuanced comprehension of wave–plasma interactions in astrophysical environments.

ORCID iDs

Syed Ayaz ● https://orcid.org/0000-0002-6709-1635
Gang Li ● https://orcid.org/0000-0003-4695-8866
Imran A. Khan ● https://orcid.org/0009-0004-5426-0833

References

Ayaz, S., Khan, I. A., Iqbal, Z., & Murtaza, G. 2020, CoTPh, 72, 035502
Ayaz, S., Khan, I. A., & Murtaza, G. 2019, PhPl, 26, 062101
Barik, K., Singh, S., & Lakhina, G. 2019a, PhPl, 26, 022901
Barik, K., Singh, S., & Lakhina, G. 2019b, URSB, 370, 17
Barik, K., Singh, S., & Lakhina, G. 2019c, PhPl, 26, 112108
Barik, K., Singh, S., & Lakhina, G. 2020, ApJ, 897, 172
Barik, K., Singh, S., & Lakhina, G. 2021, ApJ, 919, 71
Barik, K., Singh, S., & Lakhina, G. 2023, ApJ, 951, 53
Barik, K., Singh, S., & Lakhina, G. 2024, AdSpR, 73, 6041
Bostrom, R. 1992, ITPS, 20, 756
Cairns, R., Mamum, A., Bingham, R., et al. 1995, GeoRL, 22, 2709
Chen, L., & Wu, D. 2012, ApJ, 754, 123
Cramer, N. F. 2011, The Physics of Alfvén Waves (New York: Wiley)
De Moortel, I., & Browning, P. 2015, RSPTA, 373, 20140269
Dovner, P., Eriksson, A., Boström, R., & Holback, B. 1994, GeoRL, 21, 1827
Duckenfield, T., Kolotkov, D., & Nakariakov, V. M. 2021, A&A, 646, A155
Effenberger, F., da Costa, F. R., Oka, M., et al. 2017, ApJ, 835, 124
Fried, B. D., & Conte, S. D. 2015, The plasma dispersion function: the Hilbert transform of the Gaussian (New York: Academic)
Gary, G. A. 2001, SoPh, 203, 71
Gekelman, W. 1999, JGR, 104, 14417
Gershman, D. J., F-Viñas, A., Dorelli, J. C., et al. 2017, NatCo, 8, 14719
Hasegawa, A., & Chen, L. 1976, PhFl, 19, 1924
Keiling, A. 2009, SSRv, 142, 73
Keiling, A., Wygant, J., Cattell, C., et al. 2002, JGRA, 107, 1132
Khalid, M., Khan, M., Rahman, A., & Hadi, F. 2022, InJPh, 96, 1783
Khan, A. 2019, EPJP, 134, 80
Khan, I. A., Iqbal, Z., & Murtaza, G. 2020, MNRAS, 491, 2403
Khan, I. A., Iqbal, Z., Naim, H., & Murtaza, G. 2018, PhPl, 25, 082111
Khan, I. A., Khokhar, T. H., Shah, H., & Murtaza, G. 2019, PhyA, 535, 122385
Khan, I. A., & Murtaza, G. 2018, PlST, 20, 035302
Lakhina, G. 1990, Ap&SS, 165, 153
Lakhina, G. 2008, AdSpR, 41, 1688
Li, G., Shih, A. Y., Allen, R. C., et al. 2023, ApJ, 944, 196
Liu, Y., Liu, S., Dai, B., & Xue, T. 2014, PhPl, 21, 032125
Lysak, R. 2023, RvMPP, 7, 6
Lysak, R. L. 1998, GeoRL, 25, 2089
Lysak, R. L., & Lotko, W. 1996, JGR, 101, 5085
Lysak, R. L., & Song, Y. 2003, JGRA, 108, 8005
Nishizuka, N., Shimizu, M., Nakamura, T., et al. 2008, ApJ, 683, L83
Pierrard, V., & Lazar, M. 2010, SoPh, 267, 153
Rubab, N., Ali, S., & Jaffer, G. 2014, PhPl, 21, 063702
Shukla, N., Varma, P., & Tiwari, M. 2009, Indian J. Pure Appl. Phys., 47, 350
Singh, H. D., & Jatav, B. S. 2019, RAA, 19, 185
Smith, C. W., Vasquez, B. J., & Hollweg, J. V. 2011, ApJ, 745, 8
Stasiewicz, K., Bellan, P., Chaston, C., et al. 2000, SSRv, 92, 423
Verheest, F., & Pillay, S. 2008, PhPl, 15, 013703
Wu, D., & Chao, J. 2004, NPGeo, 11, 631
Wu, D.-J., & Chen, L. 2020, Kinetic Alfvén Waves in Laboratory, Space, and Astrophysical Plasmas (Singapore: Springer)
Wu, D.-J., Chen, L., Wu, D.-J., & Chen, L. 2020, Kinetic Alfvén Waves in Laboratory, Space, and Astrophysical Plasmas, 1
Wygant, J., Keiling, A., Cattell, C., et al. 2000, JGR, 105, 18,675
Wygant, J., Keiling, A., Cattell, C., et al. 2002, JGRA, 107, 1201
Zank, G. 2017, Kappa Distributions (Amsterdam: Elsevier), 609
Zhao, J., Wu, D., & Lu, J. 2010, JGRA, 115, A12227
Zirin, H. 1996, SoPh, 169, 313